Available online at www.sciencedirect.com
SCIENCE DIRECT®
ELSEVIER
Fluid Dynamics Research 35 (2004) 1–21
FLUID DYNAMICS RESEARCH

On the three-dimensional structure of the inertial wave field in a rectangular basin with one sloping boundary

Astrid M.M. Manders*, Leo R.M. Maas

Netherlands Institute for Sea Research, P.O. Box 59, 1790 AB Texel, The Netherlands

Received 16 June 2003; received in revised form 13 February 2004; accepted 25 March 2004
Communicated by T. Mullin

Abstract

Inertial waves propagate obliquely through a rotating fluid with an angle with respect to the rotation axis that is determined by the ratio of wave frequency and rotation frequency. This constraint leads to wave focusing or defocusing upon reflection at a sloping wall. In an enclosed basin repeated reflection may lead to standing waves or wave attractors: limit cycles to which all energy converges. In a two-dimensional setting (including the rotation-axis), wave patterns can be predicted mathematically; in three dimensions this is not generally possible, but ray-tracing indicated that attractors can still be found due to refractive trapping in the along-channel direction. Two wave attractors and a standing wave were investigated experimentally in a rectangular basin with a sloping wall, using particle image velocimetry. Wave attractors and a standing wave were indeed observed, with inhomogeneous energy and phase distribution in the along-channel direction, different for the different attractors and the standing wave. This behaviour can be partly understood using ray-tracing. Scale estimates revealed that the width of the attractor is limited by nonlinear advection.

PACS: 47.35+i; 47.54+r

Keywords: Inertial waves; Pattern formation; Wave attractors

1. Introduction

Homogeneous, solidly rotating fluids are stably stratified in angular momentum. They can carry waves for which motion is purely in the interior of the fluid, when the wave frequency is smaller than

* Corresponding author. Tel.: +31-222-369412; fax: +31-222-319674.
E-mail address: a.manders@basement.nl (A.M.M. Manders).

0169-5983/$30.00
doi:10.1016/j.fluiddyn.2004.03.004

twice the rotation frequency (Greenspan, 1968) and these are called inertial or gyroscopic waves. These waves are potentially relevant for the liquid outer core of the earth (Malkus, 1968; Aldridge and Lumb, 1987; Aldridge et al., 1989; Rieutord, 1995), spinning spacecraft that contain tanks filled with fluid (Aldridge et al., 1989; Manasseh, 1993), and in homogeneous layers in the ocean (van Haren and Millot, 2003). In oceans (Maas, 2001), lakes (Fricker and Nepf, 2000) and stars (Dintrans et al., 1999) they may also be modified by a stable density stratification and then occur as inertio-gravity waves.

An important property of inertial waves is that their direction of propagation is constrained to a double cone with its centre line parallel to the rotation axis. This direction is purely determined by the ratio of wave frequency and rotation frequency and cannot be altered upon reflection. When inertial waves reflect at a sloping boundary, they may become focused or defocused, depending on the slope of the boundary and the angle of propagation, as the cone has no symmetry with respect to this slope. This has important consequences for wave propagation in enclosed fluids. For a quasi-two-dimensional setting (vertical cross section of an infinitely long channel), repeated reflection with focusing may lead to the appearance of wave attractors: limit cycles onto which all wave energy converges (Stewartson, 1971; Maas and Lam, 1995). Such inertial wave attractors were theoretically predicted for cross sections of a spherical shell (Stewartson, 1971, 1972; Rieutord and Valdettaro, 1997) and were predicted and for the first time experimentally observed for a rectangular tank with one sloping side wall by Maas (2001) and Manders and Maas (2003), hereafter referred to as M and MM. These attractors behave differently from the standing waves for which focusing does not occur (horizontally positioned rectangular tanks or cylinders rotating around their axis) or for which focusing is exactly compensated by defocusing at a subsequent reflection. The consequence of the latter is that in a two-dimensional setting every individual wave ray returns onto itself (Maas and Lam, 1995). Further, the attractors exist over parameter intervals (Israeli, 1972) bounded by frequencies for which the attractor degenerates into a line or for which two coexisting attractors merge, whereas the standing waves exist at most for isolated parameter values.

However, the ‘channels’ employed in the laboratory by M and MM were necessarily of finite extent. A two-dimensional approach is therefore, strictly speaking, not justified. It is the aim of the present work to clarify the influence of the front and end wall. This issue is addressed by both a ray-theoretical and an experimental approach. The ray approach (Section 2) shows that wave focusing in the cross-slope direction is accompanied by refractive wave trapping in the along-channel direction. For a wave attractor, this implies that almost all rays penetrate only a finite distance into the channel. The experimental set-up, described in Section 3, employs a similar shape as those used in M and MM, but its smaller size enables a full camera coverage of the horizontal cross sections. The observed horizontal structure of the wave field for two attracting regimes and a non-attracting regime (Section 4) is interpreted (Section 5) using the predicted wave ray behaviour. A comparison with previous results suggests that geometric focusing of inertial waves is balanced by nonlinearities rather than viscous spreading.

2. Theory

In this section plane inertial waves will be discussed, starting from the Poincaré equation. Quasi-two-dimensional solutions are discussed briefly. Then reflection of these waves at a (sloping) wall is

described explicitly, including refraction upon oblique incidence. Finally, wave rays in an enclosed tank are traced numerically.

We consider a homogeneous, inviscid fluid rotating around a vertical axis. The basic equations governing the fluid's behaviour are the momentum equations and the continuity equation. In this paper we will consider waves in a frame of reference that is nearly in solid body rotation. The angular velocity of the frame will be $\Omega = \Omega_0 + \varepsilon\Omega_1(t)$, where Ω_0 is the background rotation rate while $\Omega_1(t) = \Omega_0 \sin(\omega t)$ is its time periodic modulation. The strength of the periodic modulation ε determines the scale of the perturbations. For $\varepsilon \ll 1$, the momentum equations can be linearized, resulting in equations for the perturbation pressure and perturbation velocities. The gradient of the pressure P and gravitational and centrifugal forces form a dynamic equilibrium at zeroth order. The remaining forces at first order due to rotation and modulation of the frame are the restoring Coriolis force and the Euler bodyforce, respectively (Tolstoy, 1973). In the inviscid description followed here, the sole condition at the boundaries is one of impermeability (vanishing normal velocities). For a more detailed description including the explicit equations we refer to MM.

The flow field will be split into two parts, a particular solution of the forced equations and a solution for the homogeneous part. The vertically uniform Euler force induces an alternating horizontal, vorticity-conserving flow. Using the shallow water approximation its horizontal structure for the tank with sloping side-wall can be calculated (MM). This alternating flow has a cross-slope component at the sloping wall near the end walls of the tank, which needs to be compensated by inertial waves of frequency ω. Inertial waves are also forced through Ekman pumping and suction via the viscous boundary layers (Greenspan, 1968; Aldridge and Toomre, 1969). But the inviscid mechanism is thought to be more important here, whereas it does not exist in rotationally symmetric containers. A plot of the theoretical flow field and details about the practical implications for the observations are presented in Section 4. Inertial waves, the subject of this study, are described by the homogeneous equations. The exact way in which the forcing drives these waves is not further resolved, since the equilibrium wave field is expected to be mainly determined by the basin shape and frequency, and to a lesser extent by the generation mechanism.

Therefore, from now on we consider the case that the fluid is rotating uniformly with constant angular velocity Ω_0. Assuming all variables to be proportional to $\exp(-\mathrm{i}\omega t)$, the momentum and continuity equation can be reduced to a single equation for the perturbation pressure p:

$$p_{xx} + p_{yy} - \lambda^2 p_{zz} = 0 \tag{1}$$

with

$$\lambda^2 = \frac{4\Omega_0^2 - \omega^2}{\omega^2} \tag{2}$$

in a Cartesian frame with z positive pointing along the frame rotation vector. For positive values of λ^2 ($\omega < 2\Omega_0$), this equation is called the Poincaré equation, in honour of H. Poincaré (Cartan, 1922). Separation of variables is only possible for limited classes of basin shapes (rectangular, cylindrical and spherical). For other basins with sloping walls, this equation cannot be solved in a straightforward way, which is precisely the problem that we meet here.

2.1. Plane wave solutions

We consider plane waves $p(x, y, z) \propto \exp(\mathrm{i}\mathbf{k} \cdot \mathbf{x})$ of arbitrary small amplitude, with $\mathbf{k} = (k_1, k_2, k_3)$ the wavenumber vector of magnitude κ. From Eq. (1) this yields

$$\lambda^2 = \frac{k_1^2 + k_2^2}{k_3^2} = \tan^2 \psi, \tag{3}$$

stating that the wavenumber vector makes an angle ψ with respect to the rotation axis, as is illustrated in Fig. 1. Together with the definition of λ (2), this implies that the wave frequency and the direction of the wavenumber vector angle are related via the ratio of angular and wave frequency, regardless of the wavenumber magnitude. The angle ϕ, the angle of the horizontal component of the wave vector with the positive x-axis, is not restricted. So the wave vector lies on a cone with half-opening angle ψ and is alternatively written as $\mathbf{k} = \kappa(\cos\phi \sin\psi, \sin\phi \sin\psi, \cos\psi)$ (Fig. 1).

The group velocity vector, $\mathbf{c}_\mathrm{g} = -(\omega/\kappa^2)(k_1, k_2, -\lambda^2 k_3)$, is perpendicular to $\mathbf{k}$, with opposite horizontal component. The angle θ of the group velocity vector with the rotation axis is directly related to λ according to $\tan^2\theta = 1/\lambda^2$. Wave energy propagates along lines (wave rays) that are in the same direction as the group velocity vector. In analogy to the wave vector, the direction of the group velocity vector (wave rays) can be given as $(\cos\phi_\mathrm{g} \sin\theta, \sin\phi_\mathrm{g} \sin\theta, \cos\theta)$. Crests and troughs propagate away from the rays with rapidly diminishing amplitude.

Regarding the chosen definition of ψ and θ, downward propagating waves will have negative values of ψ and θ, upward propagating waves will have a positive value. The absolute value of ψ and θ is conserved upon reflection. The term reflection will include refraction in the horizontal (change of ϕ and ϕ_g).

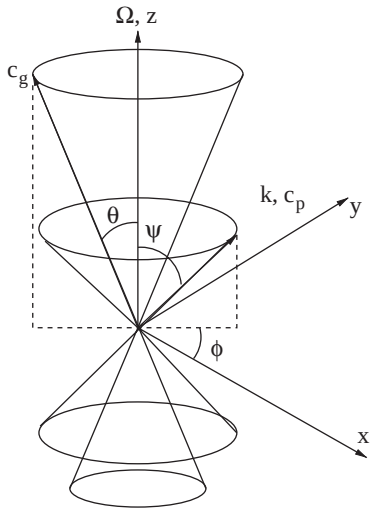

Fig. 1. Directions of wave vector, phase velocity vector and group velocity vector.

2.2. Solution in two dimensions

For a cross section of a channel that is uniform in one of the horizontal directions (y), a two-dimensional approach seems justified. For waves propagating in the cross-channel direction ($k_2 = 0$ and $\phi = 0$), the Poincaré equation reduces to the wave equation, albeit in two spatial coordinates instead of in time and space. The resulting problem is a boundary value problem. The waves still obey the above conditions regarding the constraint on the direction of propagation, and particle motion remains three-dimensional due to the Coriolis force.

For some basin shapes (horizontally placed rectangle, circle), the wave equation is easily solved using separation of variables. For basins with sloping walls this is generally not possible. Then, in two dimensions the method of characteristics can be used (John, 1941, 1978). These characteristics can be identified with the spatial paths of the wave rays (Maas et al., 1997) since time has been eliminated. Using these characteristics, the solution (pressure) in the basin can be constructed for a given pressure distribution on the boundary of the basin. For the moment we only deal with wave rays and study their spatial structure, keeping in mind that this structure forms the framework of the true solution.

The constraint on the direction of the wave has the consequence that wave rays are focused or defocused when reflecting at a sloping wall, while remaining parallel. Repeated focusing may then lead to the appearance of a limit cycle, to which all wave energy is attracted, it is therefore called the *wave attractor* (Maas and Lam, 1995). This is illustrated in Fig. 2 for a cross section of the basin and frequency conditions that were used in the experiments.

Fig. 2(a) is a critical case. Wave rays with positive slope are parallel to the slope. For incident wave rays this leads to an immediate concentration of the wave rays along the slope upon reflection. Because of the special choice of the basin geometry, there is also a closed wave ray, running from the upper left corner to the sloping wall and then parallel to the wall. All wave rays will become part of this closed ray, when they reach the slope. Therefore it is also called the *critical slope attractor*. Wave rays with a slightly larger slope would be reflected upslope, and would approach the vertex in successive reflections at the top and the sloping wall. The vertex acts as a point attractor, no closed ray path exists. This situation is equivalent to the progression of internal waves on a sloping beach (Wunsch, 1969; Cacchione and Wunsch, 1974). In fact, the V-shaped attractor consists of two

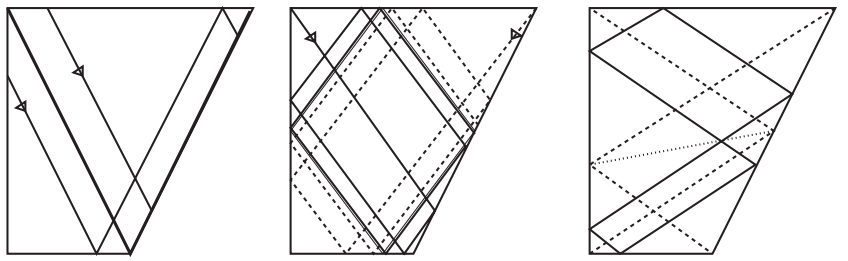

Fig. 2. Wave ray paths without refraction. (a) Critical reflection: wave rays are tangent to the slope upon reflection. (b) Focusing: every wave ray approaches the limit cycle (wave attractor) where wave energy travels in a clockwise sense. (c) Standing wave: for a single frequency all individual rays return back on themselves, and every ray intersects itself at the dotted line.

attractors: the critical slope and the degenerate form of the (1,1)-attractor, that will be described next. For the specific geometry where the bottom width equals half the top width these are connected.

In Fig. 2(b) a higher frequency (larger value of $\tan\theta$) is considered. Successive reflections at the sloping wall, where downward reflection implies focusing, bring the wave ray closer to the central parallelogram. This holds for any ray of this slope for the presented basin shape. A wave attractor is not restricted to a single angle θ but exists for a range of θ-values (window), although the parallelogram will be stretched. The window $[\theta_{\min}, \theta_{\max}]$ is bounded by $\theta = \theta_{\min}$ for which the V-shaped attractor exists, and by $\theta = \theta_{\max}$ for which a ray that starts in the upper right corner ends in the lower left corner. In this case the parallelogram has degenerated into a line. All these attractors with one reflection at the side wall and one at the top and bottom are called (1,1)-attractors, classifying the attractors by the number of reflections at the top/bottom and the (sloping) side wall (Maas et al., 1997).

In Fig. 2(c), for a still higher frequency, every individual wave ray reflects back onto itself. Focusing at downward reflection is followed by defocusing at upward reflection, no net focusing exists. In particular, wave rays which start in an upper corner end in the corner below at the same horizontal side. This case is called a standing mode and exists for a single value of θ. The periodic orbits of Fig. 2(b) are classified as (1,2) standing mode, because they reflect twice at the side walls and once at top and bottom wall.

There are several windows with attractors, and isolated values of θ with standing modes. For the standing modes, closed ray patterns have an even number of reflections at the sloping wall, and focusing will always be balanced by defocusing. The limit cycles (closed ray paths) for the attractors always have an odd number of reflections at the sloping wall, and net focusing occurs. The values of θ for which periodic ray paths exist (standing or attracting) are separated by values of θ for which no closed ray path exists and the rays fill the whole cross section. The use of characteristics and the wave attractors are described in more detail in MM.

In three dimensions however, wave rays are not identical to characteristics. But, motivated by the success of the wave rays in describing the structure of the solutions, we will study the behaviour of wave reflections in the horizontal direction. Although it is not possible to find full solutions in this way, following wave ray paths may yield elementary properties of the solutions. For this purpose, the effect of wave refraction upon reflection at a sloping wall is studied.

2.3. Refraction of plane waves

The effect of interaction with a wall on the direction of a wave ray will be described explicitly. This is most naturally done in terms of the velocity (LeBlond and Mysak, 1978) using the condition that there is no flow through the boundary. We will closely follow the notation by Phillips (1963). He used geometrical arguments to construct the reflected wave, but here the properties of the reflected wave are calculated, since this enables us to visualise the effect of reflection for the full range of possible incident waves. An alternative formulation is given by Eriksen (1982) for inertio-gravity waves.

The velocity $\mathbf{u}$ of the incident wave is given by Phillips (1963):

$$\mathbf{u}_{\text{in}} = \mathbf{a}\cos(\mathbf{k}\cdot\mathbf{x} - \omega t) + \frac{1}{\kappa}\,\mathbf{k}\times\mathbf{a}\sin(\mathbf{k}\cdot\mathbf{x} - \omega t). \tag{4}$$

The vector **a** is related to the particle motion. Its magnitude A determines the particle orbit speed (amplitude of the wave) and particle motion is in a plane perpendicular to the wavenumber vector to guarantee incompressibility. For a wave in the interior of the fluid, particles move along circles that are tangent to the cone $\mathbf{c_g}$. Apart from this constraint, the direction of **a** is arbitrary, since a shift in the direction merely implies a phase shift.

We consider reflection at a wall that makes an angle α with the rotation axis, sloping upward in the positive x-direction. Its normal **n** is then $(-\cos\alpha, 0, \sin\alpha)$. The reflected wave is given by an expression fully analogous to Eq. (4), where **b**, **m** and μ take the role of **a**, **k** and κ, respectively, including the incompressibility condition $\mathbf{b}\cdot\mathbf{m} = 0$.

The components of **m** can be calculated using the dispersion relation with the condition that the frequency is conserved and the condition that the projection of the wavenumber vector of the incoming and reflected wave on the slope must be equal. Then **b** can be calculated using the condition that there is no net motion through the boundary and the requirement that particle motion is again in a plane perpendicular to the wavenumber vector **m**.

The reflected wave has wave vector components:

$$m_1 = \frac{(\tan^2\alpha\tan^2\psi + 1)k_1 + 2\tan\alpha\tan^2\psi\, k_3}{\tan^2\alpha\tan^2\psi - 1}, \tag{5a}$$

$$m_2 = k_2, \tag{5b}$$

$$m_3 = \frac{-(2\tan\alpha\, k_1 + (\tan^2\alpha\tan^2\psi + 1)k_3)}{\tan^2\alpha\tan^2\psi - 1}. \tag{5c}$$

The transmission coefficient, the ratio $R = B/A$, with A and B the magnitudes of **a** and **b**, is more relevant in describing the action of (de)focusing than the absolute amplitude. It can be expressed as

$$\frac{B}{A} = \left|\frac{1 + \cos 2\alpha\cos 2\psi + \sin 2\alpha\sin 2\psi\cos\phi}{\cos 2\alpha + \cos 2\psi}\right|. \tag{6}$$

For an incoming wave with angle $\phi = \arctan(k_2/k_1)$, the angle of the reflected wave ϕ_{re} becomes

$$\tan\phi_{\mathrm{re}} = \frac{(\tan^2\alpha\tan^2\psi - 1)\sin\phi}{\cos\phi(1 + \tan^2\alpha\tan^2\psi) + 2\tan\alpha\tan\psi}. \tag{7}$$

For a purely horizontal or vertical wall, there is no refraction and the transmission coefficent equals 1. For arbitrary values of α, the wave is refracted, altering the value of ϕ. Also the magnitude of the wave vector will be altered upon refraction, crests and troughs will be more closely together (focusing) or further apart (defocusing).

The above calculations were all in terms of the wave vector. For ray-tracing, the direction of the group velocity vector must be considered. The angle of the group velocity with the x-axis ϕ_{g} equals $\phi + \pi$, since the horizontal components of the wave vector and the group velocity vector are opposite.

In Fig. 3(a) the ratio $\phi_{\mathrm{g,re}}/\phi_{\mathrm{g,in}}$ is plotted as function of horizontal (ϕ_{g}) and vertical (θ) incidence angles. Regions with ratio > 1 depict divergence in the y-direction, regions with ratio < 1 depict convergence. The smallest angles with respect to the positive x-direction were used to rule out the effect of propagation in the positive or negative x-direction. In the figures, $0 < \theta < \pi/2$ indicates a downward propagating incident wave, such that the upper part of the figure contains downward propagating waves (coming from above). Furthermore, for the upward propagating waves not the

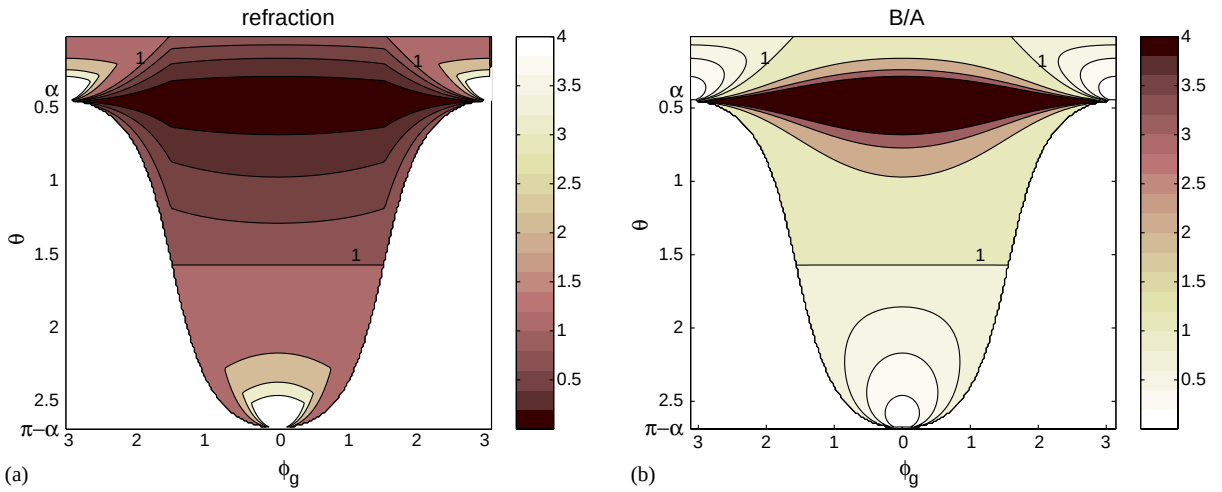

Fig. 3. Features of refraction for the slope that was used in the experiment ($\alpha = 0.45$). The unpatterned outer regions represents the parameters for which incident waves come from the back side of the slope and are therefore rejected. Here $\theta < \pi/2$ represents the *downward* propagating waves. (a) Ratio $\phi_{g,re}/\phi_{g,in}$ of the smallest angle with y=constant of the outgoing and incoming wave ray as a measure of the strength of refraction. (b) Transmission coefficient B/A. Contours are non-equidistant (0 0.25 0.5 0.75 1 2 3 4), in order to have a homogeneous distribution of contour values larger and smaller than 1.

full range of θ and ϕ_g are allowed; for values outside the bell-shaped region the rays would come from the back of the slope. The present configuration enables easy comparison with figures in MM where $\phi_g = 0$ (or π) and $0 \leqslant \theta \leqslant \pi/2$ is used to classify the parameter space. The behaviour for $\phi_{g,in} < 0$ and $\phi_{g,in} > 0$ is equivalent, there is no asymmetry for wave reflection.

In Fig. 3(b) the transmission coefficient B/A is plotted. Focusing takes place when $B/A > 1$, defocusing takes place when $B/A < 1$. This is necessary to guarantee conservation of energy flux: where wave rays are focused the wave number increases and the amplitude of the wave must increase to conserve the total energy flux. Where wave rays are defocused the wave number decreases and the amplitude must decrease.

The most important result is that wave focusing coincides with refraction towards $\phi_g = 0$ or π (cross-channel propagation). The effect is strongest for nearly critical waves ($\alpha = 0.45$ in this case). Defocusing corresponds with refraction towards $\phi_g = \pi/2$ or $-\pi/2$ (along-channel propagation).

2.4. Three-dimensional ray-tracing

Now that the effect of a single reflection has been described, we will consider the fate of wave rays that experience many reflections to investigate the possibility of limit cycles. The behaviour in an infinitely long channel is investigated: closing the channel does not alter the effect of reflection and refraction but it is less easy to see how far a wave ray has travelled before eventually reaching a limit cycle.

As a simple illustration, Fig. 4 shows rays with three different initial directions for the basin with sloping wall: (a) for subcritical reflection, (b) for the wave attractor and (c) for a standing mode. For

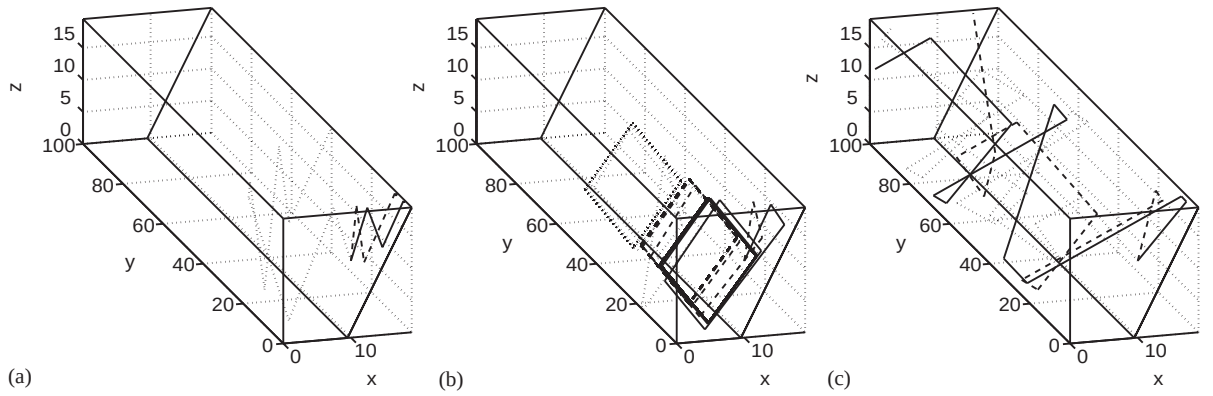

Fig. 4. Progression and convergence of wave rays starting from $(x,z)=(1,0.6)$ with $\phi_g=\pi/6$ (solid line), $\pi/3$ (dashed) and $5\pi/3$ (dotted) in a tank with sloping wall. (a) Subcritical reflection $\theta=0.42$, (b) wave attractor $\theta=0.63$, (c) standing wave $\theta=0.97$.

the first two cases, convergence in the horizontal is achieved, wave rays become part of a limit cycle. For the standing wave, rays do not converge and continue outside the depicted domain. Further, for the standing mode wave rays were observed that exhibit periodic behaviour in the y-direction: they were reflected from the corner where the bottom and sloping wall come together and the pattern is 'retraced' in an xz-projection, but still with propagation in the y-direction.

In Fig. 5, the full parameter space is investigated for a single starting position. The y-position of the wave ray after 1000 reflections is computed by numerical ray-tracing and is plotted. Light-coloured windows where most rays have converged in the y-direction (attractors) are separated by dark-coloured intervals where the majority of the rays has propagated deeply into the channel. When interpreting the figure, one must keep in mind that only the final position is indicated, which is only an indication for convergence, not convergence itself.

In a band with an attractor there are some values of ϕ_g for which the ray propagates deep into the channel before eventually converging to a fixed y-position. This occurs when the initial or refracted wave ray is nearly in the along-channel direction. This also implies that the ray reflects to the bottom and surface many times before it reflects at the slope again and can be refracted back. Some rays may reflect without ever converging in the y-direction.

Partly the features can be explained by considering the combined effect of the steepness of the rays (steeper rays are subject to stronger refraction, increasing the strength of convergence in the horizontal) and the complexity of the attractor (the simpler the structure, the larger the window of existence of the two-dimensional attractor). Consider a wave ray with angle θ_{attr} within a window of an attractor $[\theta_{min},\theta_{max}]$ and arbitrary ϕ_g. When the angle ϕ_g is reduced upon refraction such that the projection in the xz-plane $\widetilde{\theta}=\arctan c_{g,1}/c_{g,3}$ is also within this window, convergence in the y-direction and the existence of an attractor is easy to understand. Focusing in the vertical occurs at the downward reflection at the sloping wall. Upon downward reflection at this wall ϕ_g becomes closer to π, the ray is refracted more towards $y=constant$, and $\widetilde{\theta}$ is closer to θ_{attr}. For subsequent reflections this converges further till $\phi_g\to\pi$ (or 0) and $\widetilde{\theta}\to\theta_{attr}$. Then the attractor is realised and the wave is trapped at a certain y-position. If $\widetilde{\theta}$ is not in this interval, then the attractor does not 'fit'

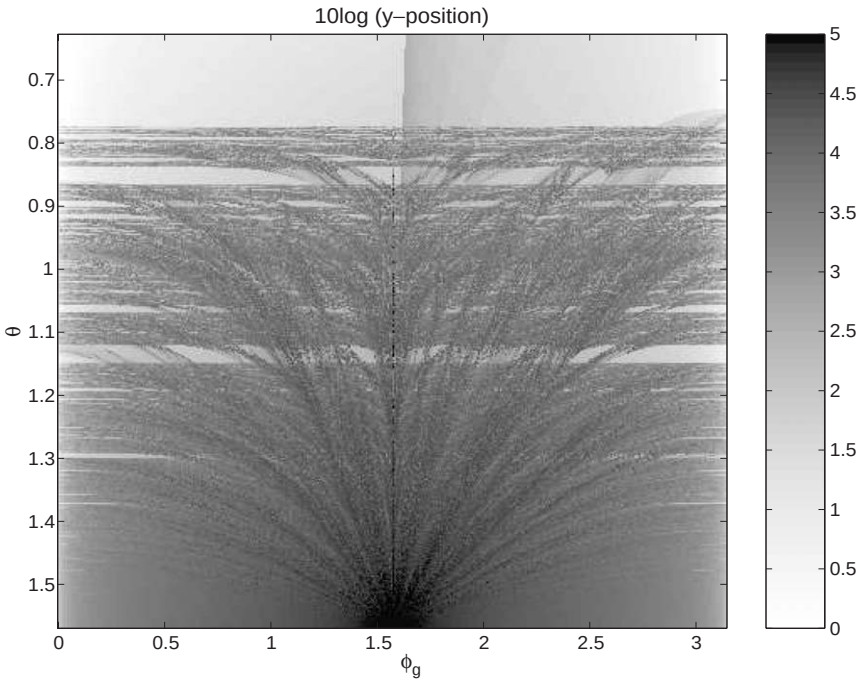

Fig. 5. Final position of wave rays after 1000 reflections in an infinitely long basin of cross section equal to that in Fig. 2, as a function of initial angles ϕ_g and θ. All rays start at the same point as in Fig. 4 in a downward direction. The subcritical reflection ($\theta < \alpha = 0.45$) and part of the (1,1)-window ($0.45 < \theta < 0.77$) are left out, since in these cases for all angles convergence was readily established.

in a two-dimensional cross section, but after a number of reflections the angle may be modified such that $\widetilde{\theta}$ is in the interval of existence of the attractor and convergence is again readily established. In contrast, for a standing mode, refraction at downward reflection is exactly balanced by refraction at upward reflection which makes it impossible to have convergence in the y-direction.

Contrary to the two-dimensional case, where all waves approached the same limit cycle, regardless of their initial position, the final position of a ray is now very sensitive to the initial position and direction. This is expressed by the speckled appearance and the narrow bands of slow convergence in windows with attractors. The attractor is no longer a single limit cycle, but a limit surface to which wave rays approach. The manifestation of a standing wave in terms of wave rays that close onto themselves becomes questionable. Periodic orbits only exist for waves that do not propagate in the y-direction. However, closing the basin may result in isolated closed rays, connecting the corners of the basin. For standing waves, these are the only closed rays apart from the ones that do not propagate in the y-direction from the beginning. For attractors these closed rays are among the rays that do not approach an attractor. Their role is as yet unclear.

Ray-tracing illustrates the possibility of trapping of wave rays on an attractor at fixed y-position. However, it is not said that such patterns are physical solutions. In a fully enclosed tank, ray analysis allows a particular ray to converge on an attractor at the vertical wall at $y = 0$. However, on the attractor, particle motion is large and also has a component in the y-direction, which violates the

boundary condition of no motion through the boundary. Only the sum of all possible rays will describe the actual wave field. The phase will determine to which amplitude they add up locally. Nevertheless, in previous experiments wave attractors have been observed, and the next sections must show their horizontal structure.

3. Experimental set-up

Experiments were performed in a perspex tank of width $2B = 19$ cm, height $H_0 = 19.5$ cm and length $L = 40$ cm. The tank was provided with a sloping wall from the top corner to half way the bottom, so that the tank effectively has bottom width B and top width $2B$, and it had a rigid lid. It was filled with homogeneous fluid (ordinary tap water), that was thus fully enclosed.

This tank was placed eccentrically on a rotating table of radius $r = 55$ cm. Fig. 6 illustrates the set-up. The rotating table had an angular velocity $\Omega_0 = 0.6912$ rad/s. This rotation rate was modulated according to $\Omega(t) = \Omega_0(1 + \varepsilon \sin(\omega t))$ to generate waves with frequency equal to the modulation frequency ω. The small parameter ε had a value of 0.1. The critical slope situation, the parallelogram shaped attractor and the (1,2)-resonant mode were investigated. Table 1 displays the forcing frequency, the ratio of wave frequency to twice the rotation frequency and $\tan\theta$.

For flow visualisation the fluid was seeded with small, almost neutrally buoyant particles. The fluid was illuminated with visible light (slide projectors) shining through a slit in the black covering of the tank. This slit had a width of about 1.5 cm. The motion was recorded by a digital camera and, via particle tracking velocimetry (van der Plas and Bastiaans, 2000), velocity fields were obtained.

Measurements were taken in horizontal cross sections (camera above the fluid, horizontal slit) and vertical cross sections (camera in front of the tank, vertical slit, as in Fig. 6). These horizontal cross sections were distributed evenly over the fluid: horizontal cross sections were taken at $z = 5$, 10 and

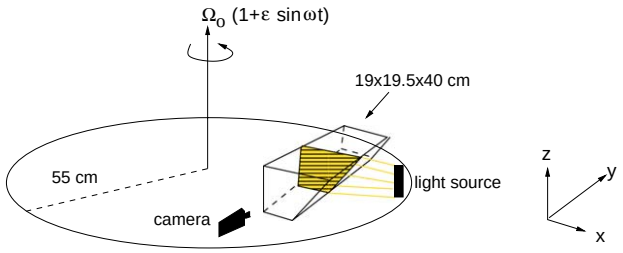

Fig. 6. Experimental set-up.

Table 1
Experimental modulation frequencies and corresponding parameter values

Name	ω	$\omega/2\Omega_0$	$\tan\theta$
Critical slope	0.6057	0.4382	0.4872
Parallelogram	0.8156	0.5900	0.7303
(1,2) standing	1.1410	0.8255	1.4617

15 cm for all frequencies. Vertical cross sections were taken at $y = 20$ and 3 cm for all frequencies. At $y = 10$ cm only the critical slope and the parallellogram shaped (1,1)-attractor were measured. The latter was measured again at $y = 30$ cm.

The frame rate of the camera was 30 Hz, which was reduced to an effective frame rate of 7.5 Hz in the processing of the data to velocity fields. The resulting time series consisted of about 240 vector fields, spanning about 33 s, so 3–6 wave periods. The particle tracking results were interpolated to obtain velocity fields on a structured grid with a spatial resolution of 0.5 cm.

A led-light was used as an indicator for the phase of the sinusoidal forcing. Knowledge of the exact phase of the data enables us to compare observations of the phases in different cross sections and to compensate for the vorticity-conserving flow. Using the theoretical prediction of the vorticity-conserving flow field, of which the strength will vary sinusoidally in time, this flow can be subtracted from the observed flow field to reveal the wave field. Its amplitude must be matched with the experimental data.

Measurements were taken some time (10 min) after onset of rotation and modulation to give the system time to evolve to what appears as a quasi-stationary state. The advantages of using such a small basin (as compared to the basins used in M and MM) are that the time for spin-up and evolution of the wave field is shorter and that the full horizontal cross section can be captured, which was not possible in the previous experiments. This enables the study of the horizontal structure of the wave field.

4. Results

The results are presented in terms of dimensionless coordinates. To facilitate comparison with MM, the same conventions are applied. This means that the scaled coordinates (x', y', z') are defined as $x' = x/B$, $y' = y/L$, $z' = z/H_0$. Primes will be dropped in the rest of the text.

The horizontal cross sections and the vertical cross section at $y = 1/10$ must be corrected for the vorticity-conserving flow (Fig. 7), since in these cross sections the vorticity-conserving flow dominates the vector field. It appeared from the observations that the strength of the vorticity-conserving flow decreased slightly with depth, instead of being constant, and that the centre of the cell, that is above the flat part of the bottom (and not at $x = 1$) shifted a little towards $x = 0$ for decreasing z. This is in agreement with the results of van Heijst et al. (1994) who also observe a shift of the centre of the inviscid circulation cell towards the vertical wall in the solutions for impulsively started flow in a wedge-shaped tank, in the case that $(H_0/L)^2$ is not much smaller than 1. For correction of the horizontal cross sections the matched amplitudes can be used. For the vertical cross section at $y = 1/10$, a linear change in amplitude with depth is used, based on the change in amplitude in the horizontal cross sections. The amplitude is then given by $A = 0.001 * z + 0.023$ with z the level in centimeters. The shift in centre position was not accounted for as it was a minor effect.

It appeared that the most dominant features in the velocity field due to the vorticity-conserving flow can be eliminated using this simple model and there is no direct need for a more sophisticated model. The remainder contained also weak vortices over the flat part of the bottom, that are also encountered in van Heijst et al. (1994), and a weak mean flow due to mixing of angular momentum near the slope, where energy is concentrated (M). Their velocities were smaller than those associated with the attractors and standing wave, and were therefore neglected in the study of the wave field.

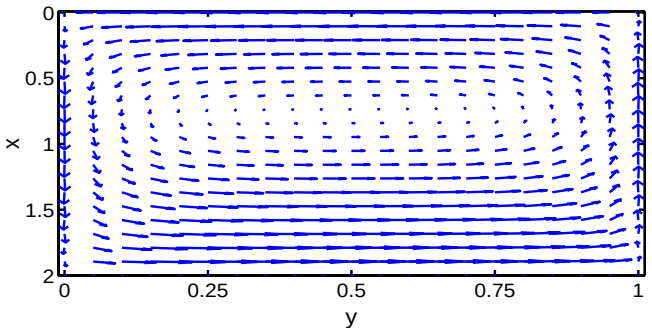

Fig. 7. Theoretical prediction of vertically uniform, vorticity-conserving flow field, based on the shallow water approximation (see MM). The slope is from $x = 1$ to 2. The flow field is not symmetric with respect to $x = 1$. The amplitude scale is arbitrary.

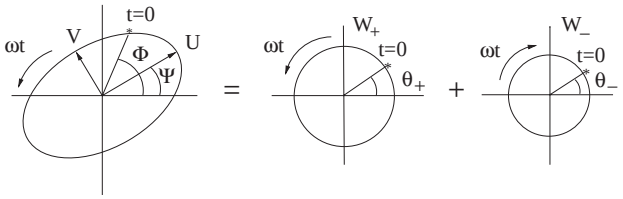

Fig. 8. Definition of ellipse parameters. The local elliptic current structure is characterised by its maximum (U) and minimum (V) radius and by its orientation Ψ and its initial phase Φ. This can be interpreted as the linear combination or two circular but counterrotating currents of the same frequency, but of amplitude $W_{\pm}$ which, at initial time, have phase angle $\theta_{\pm}$.

To analyse the wave field, time series of the tips of the velocity vectors (hodographs) were plotted. They appeared to be of elliptical shape, varying between nearly circular and nearly rectilinear. When hodographs were plotted over more than a period, patterns appear to be retraced almost exactly, which means that a stationary state is established and that the forcing frequency was by far the dominant frequency in the spectrum.

This justifies the description of the velocity field in terms of ellipse parameters, which summarise a whole time series. We characterised the ellipse by its semi-major (U) and semi-minor (V) axes, and the phases θ_+ and θ_- of the two counterrotating circular motions in which the ellipse can be decomposed (see Fig. 8, Maas and van Haren, 1987). The phase parameters do not represent the actual phase of the waves, since only projections of the three-dimensional wave field are observed, but they are used as a diagnostic tool providing insight in the phase propagation patterns and relative phases.

4.1. Vertical cross sections

Results for all the vertical cross sections are plotted together in Fig. 9. Only the intensity of the motion (U, 0.5 cm grid, in greytones) and the hodographs (1 cm grid) are plotted, since they provide most information. The hodographs are plotted over two wave periods. Their smoothness illustrates the purely periodic behaviour.

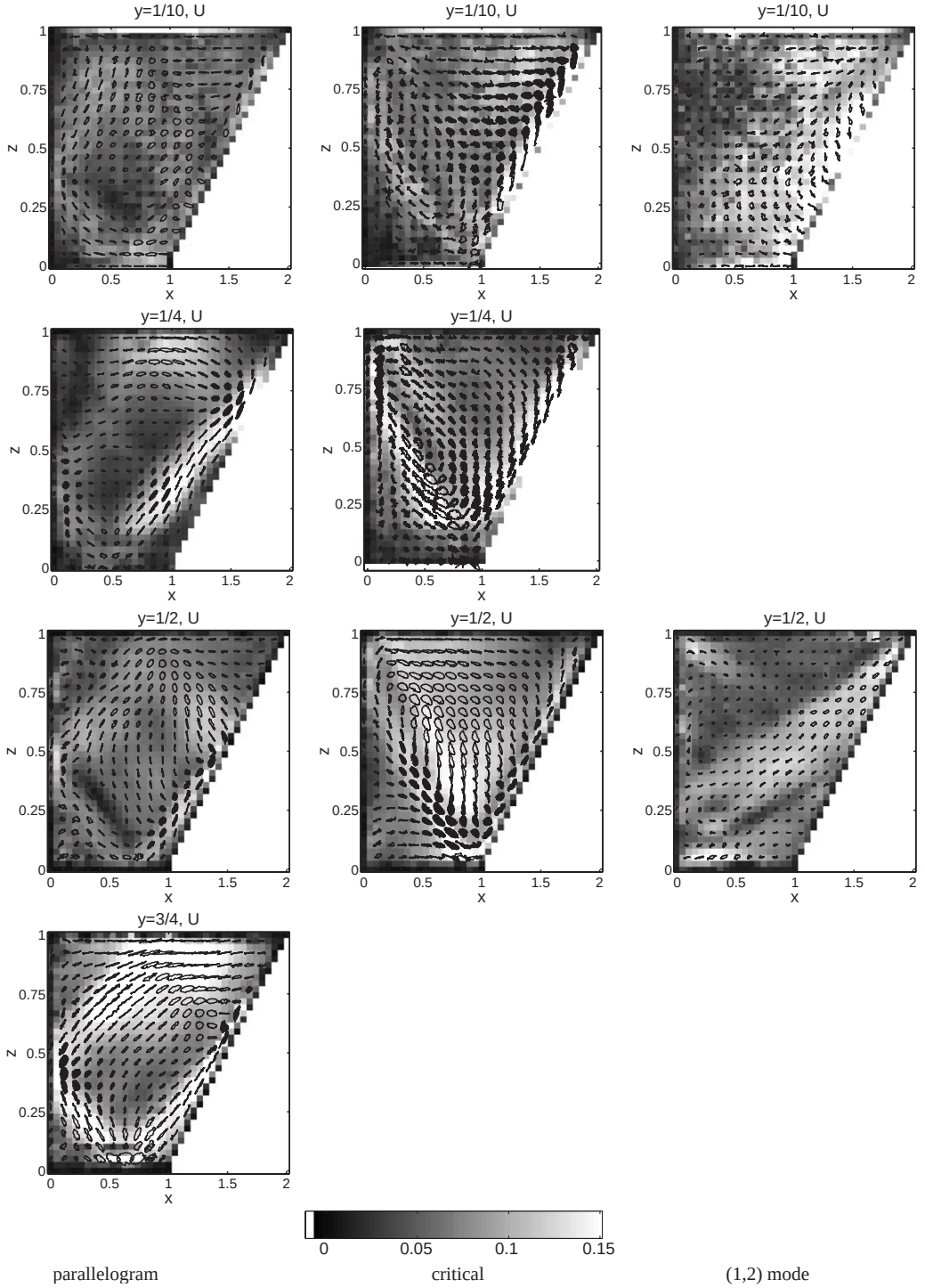

Fig. 9. Observed ellipse parameters and hodographs for the parallelogram-shaped attractor (left panel), the critical slope attractor (middle) and the (1,2) standing wave (right). Scaling for U ranges from 0 (black) to 0.15 cm/s (white) for the left and middle column, to 0.075 for the right column. Filled hodographs are traversed anticlockwise, transparent hodographs are traversed clockwise.

First, we discuss the *parallelogram shaped attractor* (Fig. 9, left column), since this (1,1)-attractor is considered the canonical form of a wave attractor. The attractor is visible at all four y-positions, but there are differences in shape and strength. Noteworthy is the relatively large circular motion in the middle at $y = 1/10$, which is absent at the other y-positions. At $y = 1/2$, the purely vertical motion in the middle is remarkable. The cross sections at $y = 1/10$ and $y = 1/4$ roughly have the same phase values (not shown), that differ nearly by π from the phases at $y = 1/2$ and $y = 3/4$. The differences in intensity and shape, the non-rectilinear hodographs along the attractor, and the phase differences between the different cross sections are indications for three-dimensional behaviour.

The triangular shape of the *critical slope attractor* (Fig. 9, middle column) can be identified in all three figures of U, although the left branch is not visible as a line of strong motion but as a line of weak motion. This is probably a result of strong shear due to opposed particle motion above and below the attractor. The hodograph patterns vary in the y-direction. Regions of clockwise and anticlockwise motion are separated by the attractor, and at $y = 1/10$ regions of clockwise and anticlockwise motion are interchanged as compared to $y = 1/2$. In between, at $y = 1/4$, the circular motion is more towards the middle, anticlockwise to the right and clockwise to the left. At $y = 1/2$, on the attractor itself the motion is nearly purely vertical, in the centre of the V-shape the ellipses are deformed such that they are curved, which points at motion with twice the forcing frequency, typical for nonlinearity. Phases are different for all three cross sections. Overall, the change of rotation sense and shape for the hodographs together with the phase changes in the along-channel direction, suggest that the wave field has a strongly three-dimensional character.

For the $(1,2)$ *standing wave* (Fig. 9, right column) motion is much weaker than for the two attractors, by about a factor two. At $y = 1/10$, only in the lower right part of the cross section the motion is substantial, there are no features typical for a (1,2) structure visible. At $y = 1/2$ these features are visible from the division in different regions with alternatingly clockwise and anticlockwise hodographs and the 'central' points of no motion ($(x,z) = (0.6, 0.2)$ and $(x,z) = (0.8, 0.65)$, cf. lines from the corners in Fig. 2). The phases θ_+ and θ_- vary only slowly at $y = 1/10$, but at $y = 1/2$ they vary clearly, being parallel to the lines connecting the corners and reproducing the pattern of U. The difference in structure between $y = 1/10$ and $y = 1/2$ makes a comparison of phases meaningless.

4.2. Horizontal cross sections

The parameters U and θ_- for the horizontal cross sections are plotted in Fig. 10, together with the hodographs. It appears that motion is dominantly clockwise such that the phase is almost fully described by θ_-. Therefore θ_+ was omitted. Only in regions of very weak motion this is not the case, but then noise may dominate. One should note that the phase increases in the direction of decreasing θ_- for clockwise motion. Near the walls, in a real fluid the velocity will be zero due to friction. However, the theoretical vorticity-conserving flow is inviscid and has maximum velocity at the walls. Subtracting the vorticity-conserving flow then gives an overcorrection, resulting in strong unphysical motion of uniform phase near the walls. Further, the measurements are slightly less accurate near the walls, since due to light reflection at the perspex walls the contrast between background and particles decreases. In the rest of the cross section the correction works well, according to the circular hodographs, since the (correction for the) vorticity-conserving flow would give rectilinear motion which is hardly ever observed.

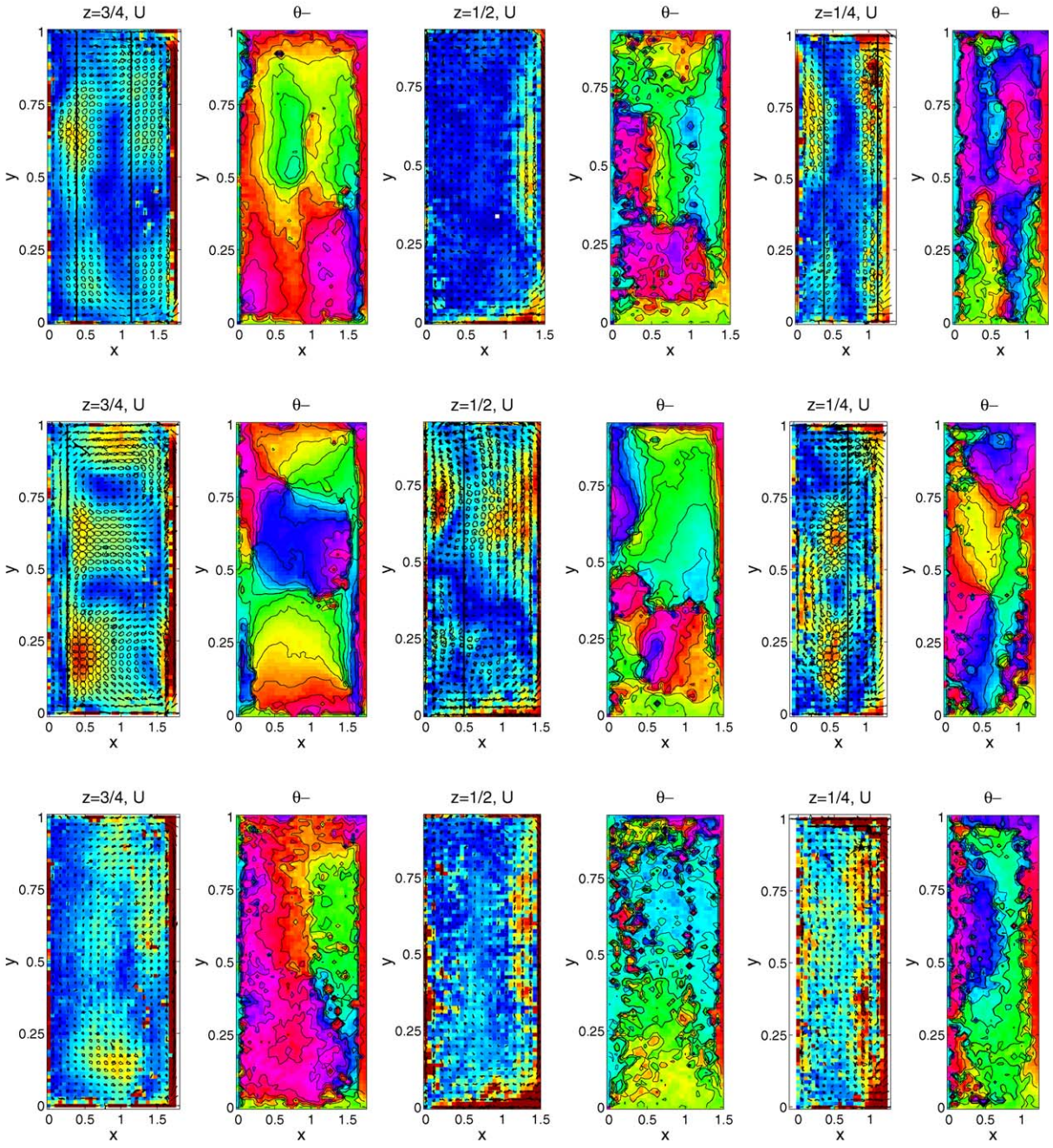

Fig. 10. Observed ellipse parameters U and θ_- in horizontal cross sections at z=3/4, 1/2 and 1/4. Also hodographs of two wave periods are plotted, transparent for clockwise motion and filled for anticlockwise motion. Upper, middle and lower panels are for modulation frequencies corresponding to the parallelogram shaped attractor, the critical slope attractor and the standing wave, respectively. The colour scale for U is from 0 (blue) to 0.2 cm/s (red) for the parallelogram and critical slope attractor, and from 0 to 0.1 cm/s for the standing mode. The phase is plotted in a cyclic color map. Black lines in the pictures of U indicate the intersection of the theoretical two-dimensional attractor with this plane.

Cross-sections of the *parallelogram shaped attractor* (Fig. 10, upper panel) clearly have four regions of stronger motion at $z = 1/4$ and 3/4. Their x-position can be associated with the location of the theoretical (two-dimensional) attractor (straight solid lines). At $z = 3/4$ the left part is in excellent agreement, at $z = 1/4$ it is the right part that coincides well with the prediction. In the middle, motion is weak. The phase pictures reproduce the four regions. In the x-direction, the phase is identical on the intersection with the attractor, reflection at the horizontal top or bottom does not alter the x and y-component of the wave. In the y-direction the phase difference between the parts $y > 0.45$ and $y < 0.45$ is about π for the sections at $z = 1/4$ and 3/4. The phase difference between $z = 1/4$ and 3/4 also nearly equals π. At $z = 1/2$ the pattern is more or less in between the patterns of $z = 1/4$ and 3/4. At $z = 1/2$ motion is weak, except near the sloping wall where the attractor reflects. Surprisingly, there the motion is strongest around $y = 1/2$ and 0. The phase picture does not exhibit the antisymmetric structure around $y = 0.45$. In general, the hodograph structure is in agreement with the vertical cross sections.

The horizontal cross sections of the *critical slope attractor* (middle panels) have a completely different structure. There are regions of strong circular motion, at $z = 3/4$ and 1/4, which have their maximum close to the theoretically predicted attractor. But there are also nearly motionless regions. Hodographs are more or less aligned around these regions. Phase lines tend to come together in the motionless, so-called amphidromic points, most clearly visible at (x, y)=(0.6,0.8) at $z = 3/4$ and (0.6, 0.4) at $z = 1/4$. The phase pattern at $z = 3/4$ suggests propagating waves with a wave length of about 1/2 in the y-direction. At $z = 1/2$ the structures are difficult to interpret. At $z = 1/4$ the structure is dominated by the amphidromic point. This point also corresponds with the purely vertical motion observed in the cross section at $y = 1/2$ around $(x, z) = (1, 0.25)$ (Fig. 9, middle column).

The $(1, 2)$ *standing wave* (bottom panel) is weaker than the two attractors, as also observed in the vertical cross sections. Motion is strongest near the sloping wall, and around $(x, y) = (0.8, 0.15)$ at $z = 3/4$ but there are no such prominent 'gaps' in the y-direction like for the two attractors. One can see smooth phase changes in the x-direction, as already noticed in the vertical cross section, but in the y-direction the phase is nearly uniform. Because the motion is so weak, the effects of noise become more important, resulting in more irregular patterns. However, the large scale structures are still coherent, which gives the results more credit.

5. Discussion

The observed wave fields showed three-dimensional behaviour for the three different frequencies. This behaviour was not only frequency-dependent in vertical cross sections, but also in the horizontal. In this final section, the results are interpreted and compared with results from ray-tracing, previous experiments and theoretical solutions for a horizontal rectangular tank. Also an estimate will be given of the process that determines the width of an attractor, using present results and observations from earlier experiments.

5.1. The three-dimensional wave field

The *parallelogram shaped attractor* was clearly visible, with maximum intensity near $y = 1/4$ and 3/4 and a phase difference of π in the y-direction with the transition at $y = 0.45$, which is a new

observation. Ray-tracing predicts the formation of limit cycles when two-dimensional theory predicts the existence of an attractor. Energy is then concentrated due to focusing upon downward reflection combined with convergence in the horizontal due to refraction. The observed high intensities at $y = 1/4$ and 3/4 suggest to be the result of such horizontal convergence of the wave rays generated at $y = 0$ and 1 (where the vorticity-conserving flow has the strongest cross-slope component). This is supported by similar observations in the larger tank (MM), where the attractor was strongest near $y = 0.12$ and waned towards $y = 0.5$, with uniform phase. In contrast, for forcing with a paddle, that was attached to the vertical wall and extended over the full length of the tank, the attractor became stronger towards the centre, $y = 0.5$, as discussed there. Furthermore, the generation mechanism would imply a phase difference of π between $y < 0.5$ and $y > 0.5$, as observed.

Near the wall at $y = 0$, the attractor was hardly visible, although the generation should be strongest there. This may be due to an adaptation to the end walls. Particle motion of inertial waves is necessarily three-dimensional, which prevents the existence of a real attractor in the vicinity of the end walls. It would be interesting to consider the structure of an ensemble of rays, starting at different points (ideally related to the generation mechanism) and propagating in different directions, and test if there are regions where the majority of rays have their limit cycle. Still, for a physically realistic solution, information about the generation and phase of the waves must be included to find the superposition of all waves, for example to describe the uniform phase over half the basin's length. Thus ray-tracing is no substitute for solving the Poincaré-equation. It appears that motion in the part $y > 0.45$ is stronger than for $y < 0.45$, and that the phase jump does not occur exactly in the middle. We have no satisfactory explanation for this. Contrary to Rossby waves, inertial waves do not have an asymmetry with respect to eastward or westward propagation.

The shape of the *critical slope attractor* is visible in all xz-cross sections, even at $y = 1/10$, which is a new observation. Motion is relatively strong, which is probably due to the immediate focusing at the sloping wall together with immediate trapping in the y-direction when a ray reflects at the slope. The interchange of locations with clockwise and anticlockwise motion (open versus filled ellipses, Fig. 9) between the sections of $y = 1/10$ and 1/2 and the in-between situation at $y = 1/4$ is remarkable. In the horizontal sections, the variation is even more clear and the rich structure could not be observed so well in MM. For this attractor there is phase propagation in the y-direction: from the interior ($y = 1/2$) towards the walls at $y = 0$ and 1. This implies energy propagation from the end walls (generation area) into the interior. The wave length seems to be 1/2 in this direction, although patterns are not symmetric with respect to 1/2. In MM it was also observed that the critical slope attractor was strong and that there was phase propagation (and energy propagation) in the y-direction. There the wave length was estimated to be 1/4 or 1/5. These wave lengths may be related to the horizontal aspect ratio of the tank, $2B/L$, which gives 0.475 for the actual basin and 0.214 for the larger tank, which are close to the observed wave lengths. Possibly the phase pattern is mainly determined by the distance over which the wave has travelled from the generation area before converging towards an attractor. Since convergence is immediate, the local structure is probably determined by a smaller number of wave rays, enabling a small-scale structure.

The $(1, 2)$-*standing wave* has the weakest motion and the most simple structure in the y-direction. The relatively weak motion can be explained by the fact that wave rays do not converge; not due to focusing due to downward reflection, nor due to refraction in the y-direction. Only wave rays that do not propagate in the y-direction, and possibly some isolated rays, can return back onto themselves. At this point it must be mentioned that the role of rays that close onto themselves, as pointed out

in the two-dimensional approximation, may not have its equivalent in three dimensions. Rieutord et al. (2001) show that the frequency belonging to the first axisymmetric mode in a full sphere does not yield periodic wave rays.

5.2. Mode solutions

The patterns in the horizontal plane of observation have some features in common with those computed for inertial waves in a horizontal rectangular tank by Maas (2002). The nearly vertical motion in the centre of the tank (Fig. 9) was also encountered in sloshing modes in the rectangular tank. In such a tank, no focusing takes place and separation of variables can be applied. Assuming standing waves in the vertical, the horizontal structure is then determined by an infinite sum of *inertial* Poincaré and Kelvin waves (no gravity). Motion for the standing wave solutions is dominantly clockwise, except in amphidromic points and near the boundaries at $y = 0$ and 1, where patterns and intensities can vary drastically on small scale. It is possible that these scales are not resolved in our measurements. The (1,2)-standing wave has a horizontal structure that resembles mode-1 solution of the rectangular tank. Overall, the increase of complexity of the horizontal structures with decreasing frequency in our observations is also present in the theoretical results of Maas (2003). For decreasing frequency, rays are steeper in the vertical, resulting in smaller horizontal structures. However, the solutions presented in Maas (2003) cannot correctly describe the solutions of the tank with a sloping wall, since focusing and wave refraction are impossible in the horizontal rectangular tank, and play an important role in the observations.

5.3. Limitation of energy concentration

It is interesting to directly compare the present observations with previous observations in larger basins by M ($54 \times 40 \times 120\ \mathrm{cm}^3$), and MM ($107 \times 80 \times 500\ \mathrm{cm}^3$) with respect to the relative thickness of the attractor. Because of the difference in scales, such a comparison reveals which processes balance the infinite concentration of energy predicted by linear theory. In Fig. 11 the values of U are plotted, divided by the maximum value $U_{\max}$ on the attractor. The different basins were plotted at the same size to enable observation of the relative width. Values smaller than $1/e$ are black. The relative width of the attractor appears to be comparable.

There are two processes which may determine the thickness of the attractor: viscous processes and nonlinear processes. Rieutord et al. (2001, 2002) investigated the width of the attractor assuming viscous processes to be the limiting factor, and found that it depended on a power of the Ekman number $E = 2\nu/(fH_0^2)$ with ν the molecular viscosity, according to $E^{1/3}$ (thinnest layer, Rieutord et al., 2001) or $E^{1/4}$ (strictly two-dimensional approach, Rieutord et al., 2002). The three different series of experiments have different Ekman numbers, as indicated in the figure and Table 2. But taking into account the length scales of the basin, as in Fig. 11, the attractor width appears to be independent of E.

Therefore we argue that nonlinear processes determine the width of the attractor in the experiments of Fig. 11, rather than viscous processes. To test this idea, the strength of the nonlinear and viscous term were estimated. As a length scale we take the distance b over which the motion increases from $U/U_{\max} = 1/e$ to 1. $U_{\max}$ is used as a velocity scale and the forcing period T as a time scale. The nonlinear terms are of order U^2/b, the viscous terms of order $\nu U/b^2$ (with $\nu = 10^{-6}\ \mathrm{m}^2/\mathrm{s}$) and

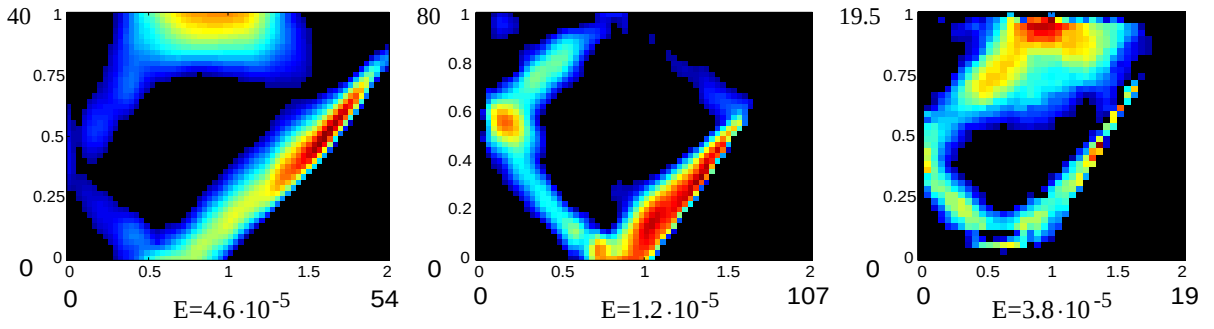

Fig. 11. Scaled maximum velocity for experiments in different sized basins. The left pictures are for basic rotation rates of 0.13 rad/s, at y-positions of 1/5 and 1/4 of the basin's length (M and MM, respectively). The rightmost figure displays the present observations at $y = 3/4$. Black parts indicate that the velocity is lower than $1/e$. Large numbers indicate the actual sizes in cm.

Table 2
Estimated scales of processes

Experiment	H_0 (cm)	E	U (cm/s)	b (cm)	$\frac{U^2}{b}$ (m/s^2)	$\frac{\nu U}{b^2}$ (m/s^2)	$2U/T$ (m/s^2)
Maas (2001)	40	4.6×10^{-5}	0.3	4.5	2×10^{-4}	1×10^{-6}	2×10^{-4}
Manders and Maas (2003)	80	1.2×10^{-5}	0.4	8	2×10^{-4}	0.7×10^{-6}	3×10^{-4}
Present	19.5	3.8×10^{-5}	0.2	1.5	3×10^{-4}	9×10^{-6}	5.2×10^{-4}

the inertial terms of order $2U/T$. Table 2 indicates that the nonlinear terms are in close agreement with the inertial terms, which means that the width of the attractor is determined by a balance between these two. The viscous term is much smaller. All of the square attractor shapes of MM have been investigated. Although at y-positions more close to the endwall ($y = 0$) the balance was slightly worse, the difference was not more than a factor two. Another argument in favour of nonlinear processes is that in M a net (Lagrangian) flow is observed, apparently resulting from mixing. Future models should therefore include nonlinear terms in the neighbourhood the mathematical attractor.

Acknowledgements

The authors thank G.J.F. van Heijst for the opportunity to use the laboratory facilities of the Fluid Dynamics Laboratory at the Eindhoven University of Technology. We gratefully acknowledge the technical support and enthousiasm of G.A.J. van der Plas during the experiments and the data processing. We appreciate the help of M.H. Rienstra and F. Eijgenraam in carrying out the experiments.

References

Aldridge, K.D., Lumb, L., 1987. Inertial waves identified in the earth's fluid core. Nature 325, 421–423.

Aldridge, K.D., Toomre, A., 1969. Axisymmetric inertial oscillations of a fluid in a rotating spherical container. J. Fluid Mech. 37, 307–323.

Aldridge, K.D., Lumb, L.I., Henderson, G.A., 1989. A Poincaré model for the earth's fluid core. Geophys. Astrophys. Fluid Dyn. 48, 5–23.

Cacchione, D., Wunsch, C., 1974. Experimental study of internal waves over a slope. J. Fluid Mech. 66, 223–239.

Cartan, M.E., 1922. Sur les petites oscillations d'une masse de fluide. Bull. Sci. Math. 46, 317–369.

Dintrans, B., Rieutord, M., Valdettaro, L., 1999. Gravito-inertial waves in a rotating stratified sphere or spherical shell. J. Fluid Mech. 398, 271–297.

Eriksen, C.C., 1982. Observations of internal wave reflection off sloping bottoms. J. Geophys. Res. 87 (C1), 525–538.

Fricker, P.D., Nepf, H.M., 2000. Bathymetry, stratification, and internal seiche structure. J. Geophys. Res. 105, 14237–14251.

Greenspan, H.P., 1968. On the inviscid theory of rotating fluids. Stud. Appl. Math. 48, 19–28.

van Haren, H., Millot, C., 2003. Rectilinear and circular inertial motions in the Western Mediterranean Sea. Oceanol. Acta, accepted.

van Heijst, G.J.F., Maas, L.R.M., Williams, C.W.M., 1994. The spin-up of fluid in a rectangular container with a sloping bottom. J. Fluid Mech. 265, 125–159.

Israeli, M., 1972. On trapped oscillations of rotating fluids in spherical shells. Stud. Appl. Math. 51, 219–237.

John, F., 1941. The Dirichlet problem for a hyperbolic equation. Am. J. Math. 63, 141–154.

John, F., 1978. Partial Differential Equations. Springer, New York.

LeBlond, P.H., Mysak, L.A., 1978. Waves in the Ocean. Elsevier, Amsterdam.

Maas, L.R.M., 2001. Wave focusing and ensuing mean flow due to symmetry breaking in rotating fluids. J. Fluid Mech. 437, 13–28.

Maas, L.R.M., 2003. On the amphidromic structure of inertial waves in a rectangular parallelepiped. Fluid Dyn. Res. 33, 376–401.

Maas, L.R.M., Benielli, D., Sommeria, J., Lam, F.-P.A., 1997. Observation of an internal wave attractor in a confined, stably stratified fluid. Nature 388, 557–561.

Maas, L.R.M., van Haren, J.J.M., 1987. Observations on the vertical structure of tidal and inertial currents in the central North Sea. J. Mar. Res. 45, 293–318.

Maas, L.R.M., Lam, F.-P.A., 1995. Geometric focusing of internal waves. J. Fluid Mech. 300, 1–41.

Malkus, W.V.R., 1968. Precession of the Earth as the cause of geomagnetism. Science 160 (3825), 259–264.

Manasseh, R., 1993. Visualization of the flows in precessing tanks with internal baffles. Am. Inst. Aeronaut. Astronaut. J. 31, 312–318.

Manders, A.M.M., Maas, L.R.M., 2003. Observations of inertial waves in a rectangular basin with one sloping boundary. J. Fluid Mech. 493, 59–88.

Phillips, O.M., 1963. Energy transfer in rotating fluids by reflection of inertial waves. Phys. Fluids 6, 513–520.

van der Plas, G.A.J., Bastiaans, R.J.M., 2000. The fptvwiz algorithm and its validation with synthetic data. Technical Report, Eindhoven University of Technology.

Rieutord, M., 1995. Inertial modes in the liquid core of the Earth. Phys. Earth Planet Interiors 91, 41–46.

Rieutord, M., Valdettaro, L., 1997. Inertial waves in a rotating spherical shell. J. Fluid Mech. 341, 77–99.

Rieutord, M., Georgeot, B., Valdettaro, L., 2001. Inertial waves in a rotating spherical shell: attractors and asymptotic spectrum. J. Fluid Mech. 435, 103–144.

Rieutord, M., Valdettaro, L., Georgeot, B., 2002. Analysis of singular inertial modes in a spherical shell: the slender toroidal shell model. J. Fluid Mech. 463, 345–360.

Stewartson, K., 1971. On trapped oscillations of a rotating fluid in a thin spherical shell. Tellus XXII (6), 506–510.

Stewartson, K., 1972. On trapped oscillations of a rotating fluid in a thin spherical shell ii. Tellus XXIV (4), 283–286.

Tolstoy, I., 1973. Wave Propogation. McGraw-Hill, New York.

Wunsch, C., 1969. Progressive internal waves on slopes. J. Fluid Mech. 35, 131–144.